HHS Public Access

Author manuscript

Phys Med Biol. Author manuscript; available in PMC 2020 September 08.

Published in final edited form as:

Phys Med Biol. ; 64(15): 15NT03. doi:10.1088/1361-6560/ab1c37.

Performance Comparison of Depth-Encoding Detectors Based on Dual-Ended Readout and Different SiPMs for High-Resolution PET Applications

Junwei Du, **Xiaowei Bai**, **Simon R. Cherry**

Department of Biomedical Engineering, University of California-Davis, One Shields Avenue, Davis, CA 95616, USA

Abstract

Silicon photomultipliers (SiPMs) are widely used in positron emission tomography (PET), however, SiPMs from different vendors vary in their performance characteristics. In addition, the specifications provided by the manufacturers are measured under different operating conditions and using different test setups, making it difficult to choose the optimal device for a specific application using the published specifications. In this work, we evaluated four state-of-the-art 8 × 8 arrays of ~ 3 × 3 mm^2 SiPMs from SensL, KETEK, and Hamamatsu for high-resolution dual-ended readout detectors using the same experimental setup and procedures. The results showed that all four SiPM arrays are excellent candidates for high-resolution PET applications, although some interesting differences in performance were noted.

1 Introduction

Silicon photomultipliers (SiPMs), also known as multi-pixel photon counters (MPPCs) and Geiger avalanche photodiodes (G-APDs), have been widely used in positron emission tomography (PET), due to their high gain, low operating voltage, high photodetection efficiency (PDE), compact form factor, insensitivity to magnetic fields and relatively low cost (Buzhan *et al* 2003 and Roncali and Cherry 2011). In the past ten years, clinical and pre-clinical PET scanners have been developed and reported both by industry and academic institutions using SiPMs from different vendors (Kwon *et al* 2011, Goertzen *et al* 2016, Grant *et al* 2016, Omidvari *et al* 2017, Berg and Cherry 2018) and research into SiPM-based PET detectors and PET scanners with improved performance continues at a rapid pace (Cherry *et al* 2017, Du *et al* 2018, Borghi *et al* 2018 and Benlloch *et al* 2018). Manufacturers are also working hard to improve the performance of SiPMs, by further reducing their noise, increasing the gain and PDE. However, every SiPM vendor has their own unique methods for fabricating SiPMs, leading to variations in properties such as microcell size, noise, and PDE (KETEK 2016b, Hamamatsu 2016 and SensL 2017). In addition, SiPMs from different manufacturers are characterized using different methods and under different conditions, which makes it difficult to choose the best SiPM for a specific PET application by comparing the published manufacturer performance specifications. Hence, SiPMs are always

jwdu@ucdavis.edu.

also evaluated by the users for their own specific applications on a case-by-case basis (Dolinsky *et al* 2015, Nemallapudi *et al* 2016 and Grodzicka-Kobylka *et al* 2017) and there are very little published data showing a direct comparison of state-of-the-art SiPM arrays tested under the same conditions.

In this paper, four of the latest generation, commercially available, 8 × 8 arrays of ~ 3 × 3 mm^2 SiPMs from three vendors (SensL, KETEK and Hamamatsu) were evaluated using the same setup and experimental methods focused on measurements relevant to high-resolution PET detectors, with the ultimate motivation and application being detectors suitable for a dedicated brain PET scanner using dual-ended readout detectors (Du *et al* 2018).

2 Materials and Methods

2.1. SiPM arrays and detector modules

Schematics and photographs of the four SiPM arrays that were tested are shown in figure 1, whilst the characteristics of the SiPM arrays are listed in table I. The reported PDEs of the SiPM arrays are shown in figure 2. The SensL SiPM array and the KETEK SiPM array both have a pitch size of 3.36 mm, whilst the two Hamamatsu SiPM arrays have a pitch size of 3.2 mm. The PDE, provided by the manufacturers, were measured at room temperature, but at different over-voltages (OV, voltage above the breakdown voltage).

To evaluate the SiPM arrays for high-resolution PET applications, four dual-ended readout detector modules were fabricated. Each detector module was assembled using two of the same SiPM arrays coupled to both ends of the same 24 × 24 array of 0.945 × 0.945 × 20 mm^3 polished LYSO crystals (Crystal Photonics, Inc., FL). The pitch size of the LYSO array was 1.0 mm and Toray lumirror E60 film (Toray Industries Inc., Japan) was used as the inter-crystal reflector (James *et al* 2009, Yang *et al* 2011 and Kuang *et al* 2018). The crystal array was coupled to the SiPM arrays using BC-630 optical grease (Saint-Gobain, S.A.) and clear acrylic sheets with a thickness of 1.0 mm were used as light guides. The BC-630 and the acrylic sheet have a refractive index of 1.465 and 1.49, respectively.

2.2. Readout electronics

Each DOI detector module has two 8 × 8 SiPM arrays with 128 SiPM pixels/signals. To simplify the readout electronics, for each array, the 64 SiPM signals were amplified individually using transimpedance amplifiers based on AD8045 chips, and the amplified SiPM signals were summed into rows and columns, generating 8 row and 8 column signals. The row/column signals were weighted by applying a gain to each row and column proportional to its location along each axis, generating four signals (X^+, X^- and Y^+, Y^-) for position information (Popov 2011). Figure 3 shows the signal multiplexing boards. Each board can handle the 64 signals from each 8 × 8 SiPM array, and the two stacked boards multiplex the 128 SiPM signals from each DOI detector module into 9 signals, 8 for position information and 1 for timing information. The timing signal was created from the sum of the 16 row and 16 column signals. The 8 signals for position information were further shaped by a CAEN spectroscopy amplifier (N586B, CAEN S.p.A., Italy) and digitized by a PowerDAQ board (PD2MFS, United Electronic Industries, Inc., USA) (Du *et al* 2018).

The gamma photon interaction position (x, y), deposited energy (E) and DOI information were calculated as follows (Du *et al* 2016 and 2018):

$$x = \frac{1}{2}\left(\frac{X_1^+ - X_1^-}{X_1^+ + X_1^-} + \frac{X_2^+ - X_2^-}{X_2^+ + X_2^-}\right),\ y = \frac{1}{2}\left(\frac{Y_1^+ - Y_1^-}{Y_1^+ + Y_1^-} + \frac{Y_2^+ - Y_2^-}{Y_2^+ + Y_1^-}\right) \quad (1)$$

$$E = E_1 + E_2 \quad (2)$$

$$DOI = a\left(\frac{E_1 - E_2}{E_1 + E_2}\right) + b \quad (3)$$

where $E_1 = X_1^+ + X_1^- + Y_1^+ + Y_1^-$ and $E_2 = X_2^+ + X_2^- + Y_2^+ + Y_2^-$ were the two energies detected by the two SiPM arrays coupled at opposite ends of the LYSO array. X_i^+, X_i^-, Y_i^+, Y_i^- (i = 1, 2) were the position signals from SiPM array i. a and b were constants used to model the relationship between the ratio of the two energies and the DOI.

2.3 Experimental methods

Identifying the optimal bias voltage for measuring the flood histogram is essential to achieve the best performance for high-resolution detectors (Du *et al* 2016 and 2018), hence, the crystal identification ability (flood histogram) of the detector modules was evaluated at different bias voltages (with an 0.5 V interval) and at four different temperatures (table II), whilst the energy, timing, and DOI resolution were evaluated at the optimal bias voltage found for each SiPM array for the flood histogram (table III). The detector module being evaluated, along with the electronics boards (figure 3), were placed in a light-tight black box and cooled using cold, dry air. The detector's temperature was monitored by a thermocouple attached to the back side of the SiPM array. A 0.25 mm diameter, 30 uCi ^{22}Na point source was used to irradiate the LYSO array, and a 350 – 750 keV energy window was applied to each crystal to select events.

Experimental methods followed the methods we have previously developed and published and are only briefly summarized here (Du *et al* 2016 and 2018).

2.3.1 Flood histograms—Flood histogram data were acquired using a reference detector consisting of a 25 mm diameter × 30 mm cylindrical LYSO crystal (wrapped with six layers of Teflon) coupled to a Hamamatsu R13449–10 PMT and a timing window of 10 ns. The distance between the source and the DOI detector was 10 cm, and the source was placed 3 cm from the reference detector. To quantitatively compare the flood histograms, a flood histogram quality metric, k, was computed by calculating the distance between adjacent crystal spots divided by the width of the crystal spots (Du *et al* 2016). The optimal bias voltage for the flood histogram was determined as the settings at which the highest value of k was obtained.

Because the Hamamatsu SiPM arrays are slightly smaller (figure 1), and the 24 × 24 LYSO array comes closer to the edges compared with the SensL and KETEK arrays, some crystals

in the last two columns could not be identified in the flood histograms. Hence the flood histogram quality was computed using only the central 20 × 20 LYSO elements for fair comparison. The energy resolution and the timing resolution were also computed using the central 20 × 20 LYSO elements.

2.3.2 Energy resolution—The energy resolution was calculated using the same data obtained for the flood histograms and energy spectra were extracted for individual crystals in the LYSO array. The energy resolution at 511 keV for each crystal was the ratio of the FWHM to the amplitude of the photopeak from a Gaussian fit to the energy spectra, expressed as a percentage.

2.3.3 Signal-to-noise ratio—The signal-to-noise ratio (SNR) was calculated for each crystal using the data obtained for the flood histograms. The signal amplitude was taken as the centroid of the Gaussian fit to the 511 keV photopeak of the energy spectrum. The noise was the FWHM of histogram of the summed eight position signals obtained by periodically triggering the DAQ board using the computer clock. The average SNR across the selected 20 × 20 crystals was calculated as the SNR of the detector module (Du *et al* 2018).

2.3.4 DOI measurements—The detector module was irradiated from the side at 5 fixed depths (2 to 18 mm, in 4 mm intervals) by using a reference detector (based on 25 mm diameter Hamamatsu R13449–10 PMT and a 0.5 × 20 × 20 mm^3 LYSO plate wrapped with Teflon) in coincidence (Du *et al* 2018). The distance from the ^{22}Na source to the reference detector was 100 mm and the distance from the ^{22}Na source to the dual-ended readout detector was 80 mm. Data was collected at different depths and DOI was calculated by comparing the two energy signals detected by the two SiPM arrays with appropriate calibration (equation 3). The FWHM of the DOI distribution was used as a measure of the DOI resolution (Du *et al* 2018). Because only some of the LYSO elements were efficiently irradiated due to the geometry, and the fact that the signal drops off quickly with distance from the side entrance face (figure 4), only the 12 × 12 LYSO elements shown in the white rectangle in figure 4 were used to compute the DOI resolution.

2.3.5 Timing measurements—Coincidence timing resolution (CTR) data were acquired using a reference detector consisting of a 16 × 16 × 16 mm^3 LYSO cube (wrapped with six layers of Teflon) coupled to a Hamamatsu R13449–10 PMT in coincidence. Timing triggers were generated using constant fraction discriminators (CFDs) (Model 584, ORTEC, TN), both for the SiPM-based detector and the reference detector and sent to a time-to-amplitude converter (TAC) (Model 566, ORTEC, TN). The delay for the CFDs used for the SiPM signal and PMT signal were 16 ns and 1 ns, respectively, with the CFD threshold set just above the noise level. The output of the TAC was digitized using an analog-to-digital converter (ADC) (PD2MFS, United Electronic Industries, Inc., MA). Timing spectra were extracted for individual crystals in the LYSO array and the FWHM of a Gaussian fit to the coincidence timing spectra (test detector in coincidence with reference detector) was taken as the CTR. The coincidence timing resolution of two identical reference detectors was 446 ± 15 ps.

3. Results

3.1 Flood histograms

Figure 5 shows the best flood histogram obtained using the different SiPM arrays at 0 °C. All the LYSO crystals can be clearly identified except some crystals in the last two rows and columns in the flood histograms obtained using the Hamamatsu SiPM arrays. As explained earlier, this is because the LYSO array extends closer to the edges of the Hamamatsu arrays due to their slightly smaller area, making it difficult to identify the outermost crystals using light sharing. The flood histogram quality metric, calculated using the central 20 × 20 LYSO elements and the method described in Du *et al* 2016, is shown in figure 6. The flood histogram quality generally increases and then decreases with increasing bias voltage, however, the responses of the SiPMs are quite different. While the Hamamatsu arrays can yield the highest values, the values also show a larger dependence on the bias voltage than these obtained using the SensL and the KETEK SiPM arrays. Better flood histogram quality was obtained at lower temperature, as expected, due to the lower SiPM noise (Piemonte *et al* 2013).

The highest flood histogram quality values obtained using different SiPM arrays at different temperatures are shown in figure 7 and the corresponding bias voltages are listed in Table III. The best flood histogram was obtained using the Hamamatsu S13361 SiPM arrays. Table III and figure 6 show that the optimal bias voltage for the flood histogram at different temperatures varies little for the SensL and KETEK SiPM arrays, but increases with increasing temperature for the Hamamatsu SiPM arrays.

3.2 Energy resolution

The average energy resolution calculated using the central 20 × 20 LYSO elements are shown in figure 8. The average energy resolution obtained using different SiPM arrays are comparable and does not change much with increasing temperature. The average energy resolution measured here, 25–27%, is poorer than other reports in the literature (Borghi *et al* 2017 and Choe *et al* 2017), because the LYSO arrays (reflector and surface treatment) were optimized to obtain good DOI information. These LYSO arrays exhibit a strong depth dependence of the 511 keV photopeak position (Ren *et al* 2014).

3.3 Signal-to-noise ratio

The average signal, noise and average SNR across the central 20 × 20 LYSO elements are shown in figure 9. They were obtained at the optimal bias voltage for the flood histogram (shown in Table III). Better SNR was obtained at lower temperatures, as expected. The best SNR was obtained using the Hamamatsu S13361 SiPMs. Interestingly, the Hamamatsu S13361, despite having slightly higher noise, gives better SNR than the Hamamatsu S14161 at these settings. This is because the working over-voltage of the Hamamatsu S13361 SiPM for the optimal flood histogram is higher than that of the S14161 SiPM, and the increase in signal at this over-voltage outweighs the higher noise levels.

3.4 DOI resolution

The average DOI resolution across the selected crystals (figure 4) and all the five depths are shown in figure 10. The average DOI resolution degrades slightly with increasing temperature. The average value of the DOI resolution obtained using different SiPM arrays are comparable, with slightly better DOI resolution obtained using the SensL and the Hamamatsu S13361 SiPM arrays.

3.5 Timing resolution

The CTR (test detector in coincidence with reference detector) averaged across the central 20 × 20 LYSO elements and obtained at different temperatures is shown in figure 11. The timing resolution obtained using different SiPM arrays degrades with increasing temperature, and the best timing resolution was consistently obtained using the Hamamatsu S14161 SiPM arrays.

4. Discussion and Conclusions

In this paper, the performance of four commercially available 8 × 8 arrays of ~ 3 × 3 mm^2 SiPMs from three leading vendors (SensL, KETEK, and Hamamatsu) were evaluated and compared in a high-resolution dual-ended readout detector module. Overall, the four SiPM arrays are all excellent candidates for high-resolution PET applications. However, due to the different properties and characteristics of the four SiPM arrays (figure 2 and table I), such as the microcell size, the gain, and the PDE, the four detector modules show some interesting performance differences.

LYSO arrays with a pitch size of 1.0 mm and a length of 20 mm can be clearly resolved by the four SiPM arrays (figure 5). Higher flood histogram quality values and higher SNR values were measured using the Hamamatsu SiPM arrays (figure 7 and 9), mainly due to the slightly smaller pitch size (table I) and the higher PDE (figure 2) of the Hamamatsu SiPM arrays. However, the flood histograms obtained with the SensL and KETEK SiPM arrays were less sensitive to bias voltage, and the SensL and KETEK SiPMs have lower operating bias voltages, which could be advantages in a scanner setting.

The energy resolution obtained using the four SiPM arrays are comparable (figure 8). The energy resolution was not corrected for saturation, as the light is spread across multiple SiPMs at both ends of the scintillator array. The energy resolution is mainly dominated by the performance of the LYSO array, due to the fabrication method and the Toray reflector which emphasized good DOI performance. Better energy resolution could be obtained using a different reflector (such as $BaSO_4$) and a different fabrication method (Stickel *et al* 2006 and Kuang *et al* 2017), or by measuring the energy spectrum as a function of interaction depth.

As expected, the DOI resolution degrades with increasing temperature, as the noise of SiPMs increases as the temperature goes up (Piemonte *et al* 2003 and Du *et al* 2016). The DOI resolution iŝ3 mm, and slightly better values were obtained using the SensL SiPM arrays and the Hamamatsu S13361 SiPM arrays.

The best timing resolution was obtained using the Hamamatsu S14161 arrays (figure 2 and figure 11). The timing resolution is around 1 ns, which is not as good as the start-of-art time-of-flight PET detectors and scanners (Grant *et al* 2016, Nemallapudi *et al* 2016 and Borghi *et al* 2018), but is still sufficient for high resolution dedicated organ and small animal PET scanners. The timing resolution is mainly dominated by the multiplexing readout method and the less than optimal light collection of the LYSO array (Aguilar *et al* 2015) which is designed to provide high DOI resolution. The timing resolution could be significantly improved by extracting the timing information from individual SiPMs, for example using an ASIC designed for SiPM arrays (Becker *et al* 2016).

The flood histograms (figure 7) and the SNR (figure 9) obtained using the SensL and KETEK SiPMs are clearly worse than those obtained using the Hamamatsu SiPMs, mainly caused by the difference in the PDE, with higher PDE corresponding to SiPMs with larger microcell size. The KETEK SiPM has the smallest microcells (Table I), hence, its PDE is the lowest among the four tested SiPMs. However, SiPMs with smaller microcells will have better energy linearity.

In conclusion, the continuous development, evolution, and refinement of SiPMs over the past decade has resulted in high-performance SiPM arrays from several vendors, all of which work well in this application. There are minor differences in performance and sensitivity to operating parameters (bias voltage and temperature), which together with cost, robustness and reliability, ultimately will guide selection for high-resolution PET scanner projects.

Acknowledgments

The authors wish to thank SensL (now part of ON Semiconductor), KETEK and Hamamatsu for providing the SiPM arrays used in this work. This work was funded by NIH grant R01 EB019439.

References

Aguilar A, González A, Torres J, García-Olcina R, Martos J, Soret J, Conde P, Hernández L, Sánchez F and Benlloch J 2015 Timing results using an FPGA-based TDC with large arrays of 144 SiPMs IEEE Trans. Nucl. Sci 62:12–18.

Becker R, Casella C, Corrodi S, Dissertori G, Fischer J, Howard A, Ito M and Lustermann W 2016 Studies of the high rate coincidence timing response of the STiC and TOFPET ASICs for the SAFIR PET scanner JINST 11:P12001.

Benlloch J, González A, Pani R, Preziosi E, Jackson C, Murphy J, Barberá J, Correcher C, Aussenhofer S, Gareis D, Visvikis D, Bert J, Langstrom B, Farde L, Toth M, Haggkvist J, Caixeta F, Kullander K, Somlai-Schweiger I and Schwaiger M 2018 The MINDVIEW project: First results European Psychiatry 50:21–27. [PubMed: 29398564]

Berg E, Cherry SR 2018 Innovations in instrumentation for positron emission tomography Seminars in Nuclear Medicine 48:311–331. [PubMed: 29852942]

Borghi G, Tabacchini V, Bakker R and Schaart D 2018 Sub-3 mm, near-200 ps TOF/DOI-PET imaging with monolithic scintillator detectors in a 70 cm diameter tomographic setup Phys. Med. Biol 63:155006. [PubMed: 29995639]

Buzhan P, Dolgoshein B, Filatov L, Ilyin A, Kantzerov V, Kaplin V, Karakash A, Kayumov F, Klemin S, Popova E and Smirnov S 2003 Silicon photomultiplier and its possible applications Nucl. Instrum. Methods A 504:48–52.

Cherry SR, Jones T, Karp J, Qi J, Moses W and Badawi R 2017 Total-body PET: maximizing sensitivity to create new opportunities for clinical research and patient care J. Nucl. Med 59:3–12. [PubMed: 28935835]

Choe H, Choi Y, Hu W, Yan J and Jung J 2017 Development of capacitive multiplexing circuit for SiPM-based time-of-flight (TOF) PET detector Phys. Med. Biol 62:N120–133. [PubMed: 28263947]

Dolinsky S, Fu G and Ivan A 2015 Timing resolution performance comparison of different SiPM devices Nucl. Instrum. Methods A 801:11–20.

Du J, Bai X, Gola A, Ferri A, Piemonte C, Yang Y and Cherry SR 2018 Performance of a high-resolution depth-encoding PET detector module using linearly-graded SiPM Phys. Med. Biol 63:035035. [PubMed: 29324437]

Du J, Yang Y, Bai X, Judenhofer M, Berg E, Di K, Buckley S, Jackson C and Cherry SR 2016 Characterization of large-area SiPM array for PET applications IEEE Trans. Nucl. Sci 63:8–16. [PubMed: 27182077]

Goertzen A, Stortz G, Thiessen J, Bishop D, Khan M, Kozlowski P, Retière F, Schellenberg G, Shams E, Sossi V and Thompson C 2016 First results from a high-resolution small animal SiPM PET insert for PET/MR imaging at 7T, IEEE Trans. Nucl. Sci 62:2424–2433.

Grant A, Deller T, Khalighi M, Maramraju S, Delso G and Levin CS 2016 NEMA NU 2–2012 performance studies for the SiPM-based ToF-PET component of the GE SIGNA PET/MR system Med. Phys 43:2334–2343. [PubMed: 27147345]

Grodzicka-Kobylka M, Szczesniak T and Moszyński M 2017 Comparison of SensL and Hamamatsu 4×4 channel SiPM arrays in gamma spectrometry with scintillators Nucl. Instrum. Methods A 856:53–64.

Hamamatsu. MPPCs for precision measurement, S13360 series Datasheet. 2016. https://www.hamamatsu.com/resources/pdf/ssd/s13360_series_kapd1052e.pdf

Hamamatsu. S13361–3050 series: MPPC arrays in a chip size package miniaturized through the adoption of TSV structure Product Datasheet. 2017. https://www.hamamatsu.com/us/en/product/type/S13361-3050NE-08/index.html

James S, Yang Y, Wu Y, Farrell R, Dokhale P, Shah K and Cherry SR 2009 Experimental characterization and system simulations of depth of interaction PET detectors using 0.5 mm and 0.7 mm LSO arrays Phys. Med. Biol 54:4605–4619. [PubMed: 19567945]

KETEK. SiPM – silicon photomultiplier array PA3325-WB-0808. Product Datasheet. 2016a. https://www.ketek.net/wp-content/uploads/2016/12/KETEK-PA3325-WB-0808-Datasheet.pdf.

KETEK 2016b SiPM - silicon photomultiplier, PM3315-WB/PM3325-WB, Product Datasheet https://www.ketek.net/wp-content/uploads/2016/11/KETEK-PM3315-WB-PM3325-WB-Datasheet.pdf.

Kuang Z, Sang Z, Wang X, Fu X, Ren N, Zhang X, Zheng Y, Yang Q, Hu Z, Du J, Liang D, Liu X, Zheng H and Yang Y 2018 Development of depth encoding small animal PET detectors using dual-ended readout of pixelated scintillator arrays with SiPMs Med. Phys 45:613–621. [PubMed: 29222959]

Kuang Z, Wang X, Li C, Deng X, Feng K, Hu Z, Fu X, Ren N, Zhang X, Zheng Y, Liang D, Liu X, Zheng H and Yang Y 2017 Performance of a high-resolution depth encoding PET detector using barium sulfate reflector Phys. Med. Biol 62:5945–5958. [PubMed: 28682792]

Kwon S, Lee J, Yoon H, Ito M, Ko G, Choi J, Lee S, Song I, Jeong J, Lee D and Hong S 2011 Development of small-animal PET prototype using silicon photomultiplier (SiPM): initial results of phantom and animal imaging studies J. Nucl. Med 52:572–579. [PubMed: 21421723]

Nemallapudi M, Gundacker S, Lecoq P and Auffray E 2016 Single photon time resolution of state of the art SiPMs JINST 11:P10016.

Omidvari N, Cabello J, Topping G, Schneider F, Paul S, Schwaiger M and Ziegler S 2017 PET performance evaluation of MADPET4: a small animal PET insert for a 7 T MRI scanner Phys. Med. Biol 62:8671–8692. [PubMed: 28976912]

Piemonte C, Ferri A, Gola A, Pro T, Serra N, Tarolli A and Zorzi N 2013 Characterization of the first FBK high-density cell silicon photomultiplier technology IEEE Trans. Electron Devices 60:2567–73.

Popov V 2011 Advanced data readout technique for multianode position sensitive photomultiplier tube applicable in radiation imaging detectors JINST 6:C01061.

Ren S, Yang Y and Cherry SR 2014 Effects of reflector and crystal surface on the performance of a depth-encoding PET detector with dual ended readout Med. Phys 41:072503. [PubMed: 24989406]

Roncali E and Cherry SR 2011 Application of silicon photomultipliers to positron emission tomography Ann. Biol. Eng 4:1358–1377.

SensL 2017 J-series high PDE and timing resolution, TSV package Datasheet http://sensl.com/downloads/ds/DS-MicroJseries.pdf.

SensL 2018 ArrayJ - high fill-factor arrays of J-Series SiPM sensors ArrayJ User Manual http://sensl.com/downloads/ds/UM-ArrayTSV.pdf.

Stickel J, Qi J and Cherry SR 2007 Fabrication and characterization of a 0.5-mm lutetium oxyorthosilicate detector array for high-resolution PET applications J. Nucl. Med 48:115–121. [PubMed: 17204707]

Yang Y, James S, Wu Y, Du H, Qi J, Farrell R, Dokhale P, Shah K, Vaigneur K and Cherry SR 2011 Tapered LSO arrays for small animal PET Phys. Med. Biol 56:139–153. [PubMed: 21119228]

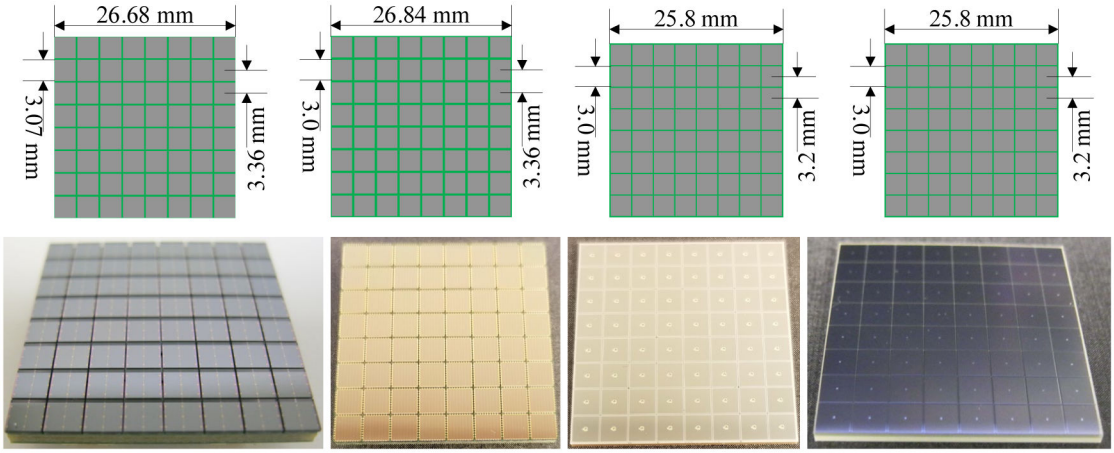

Figure 1.

(top row) schematics and (bottom row) photographs of the SiPM arrays tested. From left to right, SensL MicroFJ-30035, KETEK PA3325-WB, Hamamatsu S13361–3050, and Hamamatsu S14161–3050.

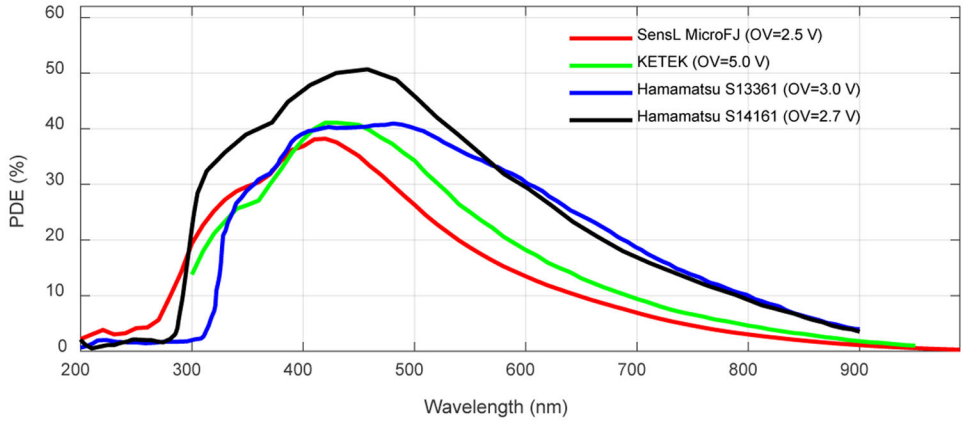

Figure 2.

PDE of the SiPM arrays versus wavelength. Data provided by the manufacturers (KETEK 2016b, Hamamatsu 2016 and SensL 2017). Note that the published PDEs were acquired at different OVs. For a given SiPM, the PDE increases at higher OV. The PDE at 430 nm of the KETEK SiPM is 31 % at an OV of 2.5 V.

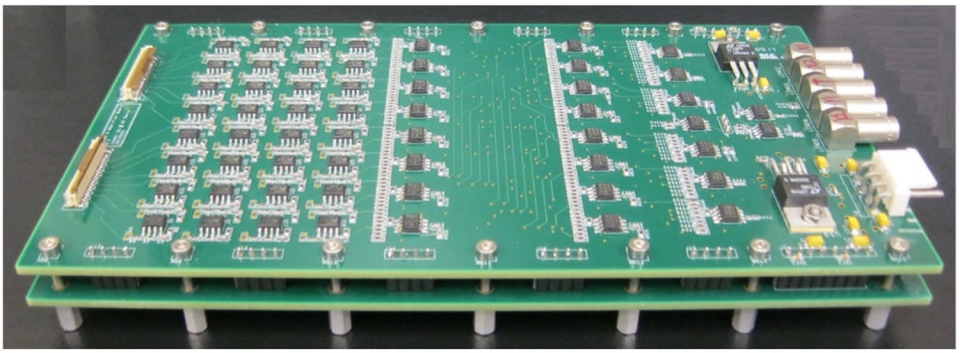

Figure 3.
Photograph of the signal multiplexing boards. Two identical boards were stacked together to handle the 128 signals from each dual-ended detector module. Each board can process the 64 signals from one 8 × 8 SiPM array.

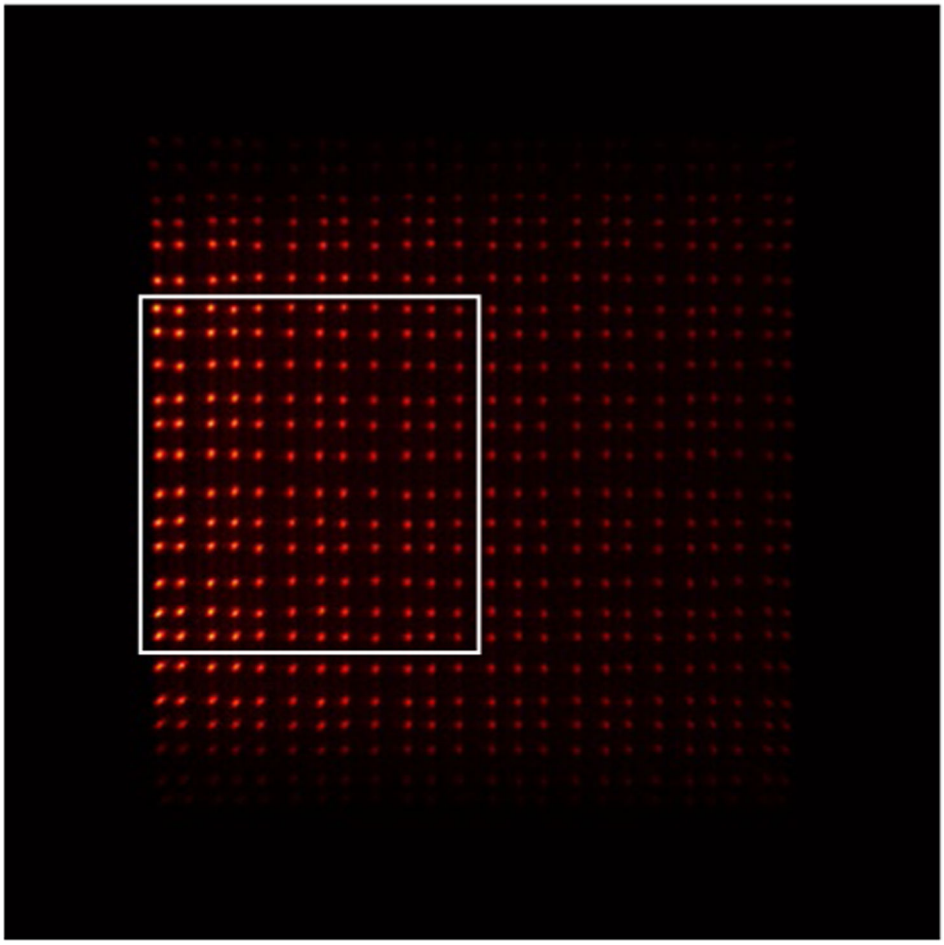

Figure 4.
Crystals shown in the white rectangle were used to calculate the DOI resolution.

Figure 5.

Flood histogram obtained using (from left to right) SensL, KETEK, Hamamatsu S13361 and Hamamatsu S14161 SiPM arrays at a temperature of (top row) 0 °C and (bottom row) 20 °C. The bias voltages were listed in Table III.

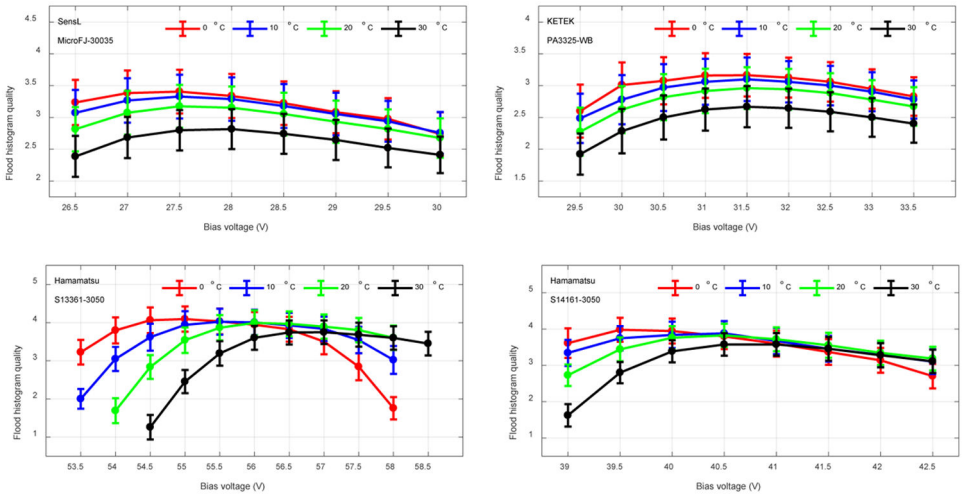

Figure 6.
Flood histogram quality versus overvoltage and temperature.

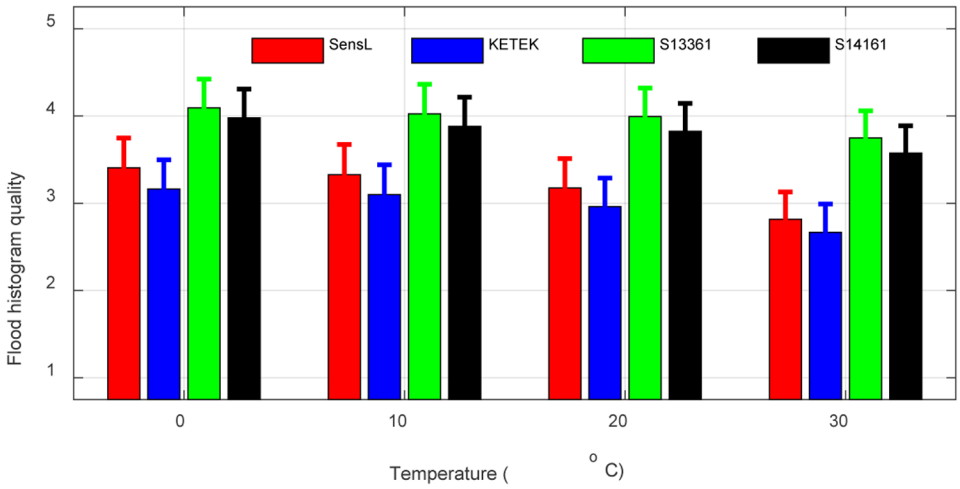

Figure 7.
Highest flood histogram quality values versus temperature.

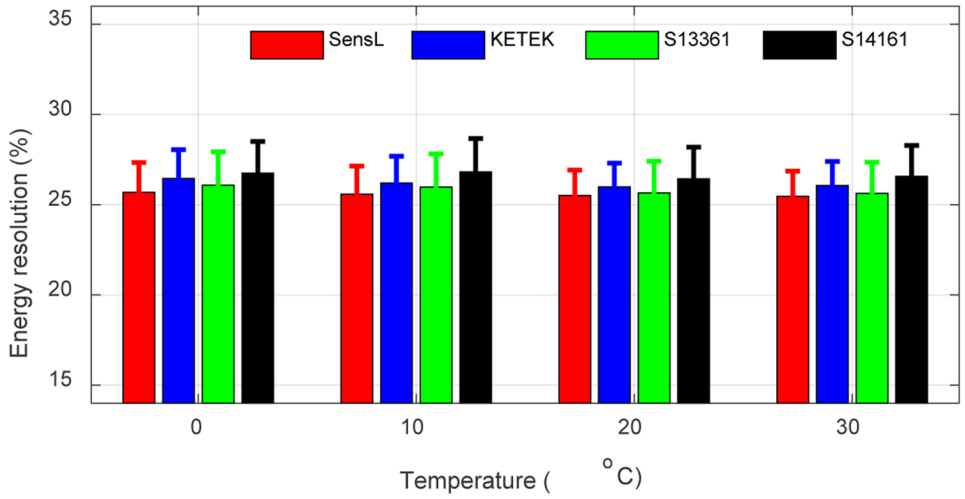

Figure 8.
Average energy resolution versus temperature.

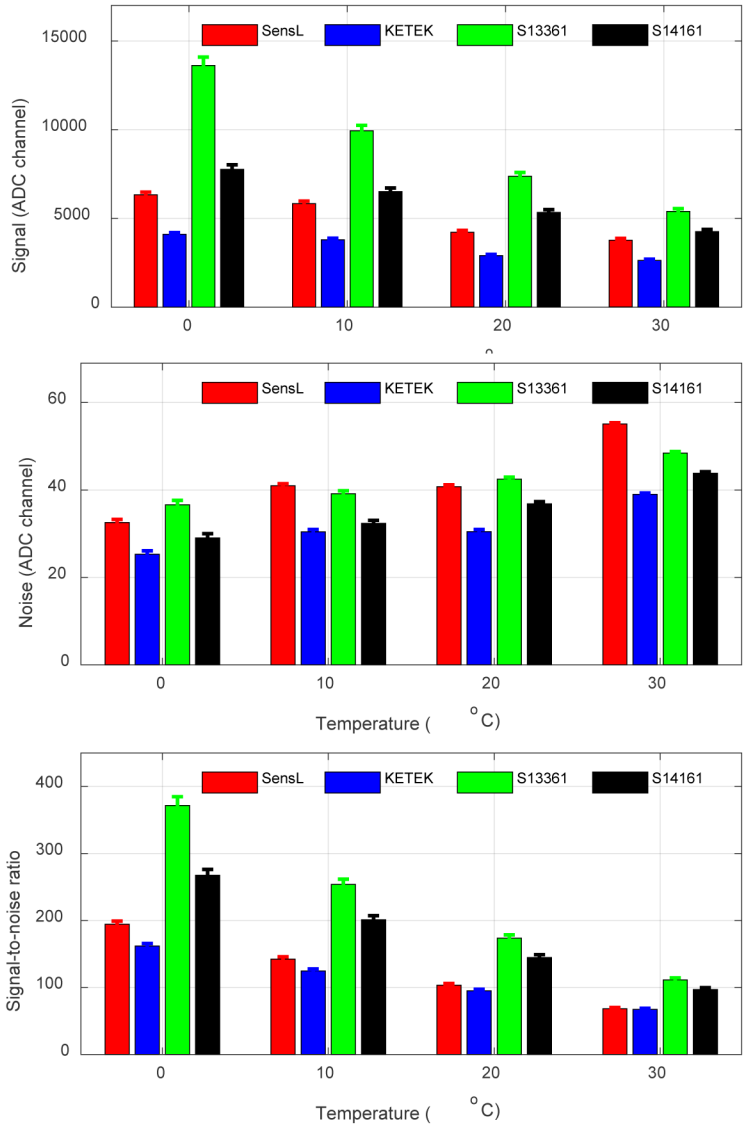

Figure 9.
(top) signal, (middle) noise and (bottom) signal-to-noise ratio versus temperature.

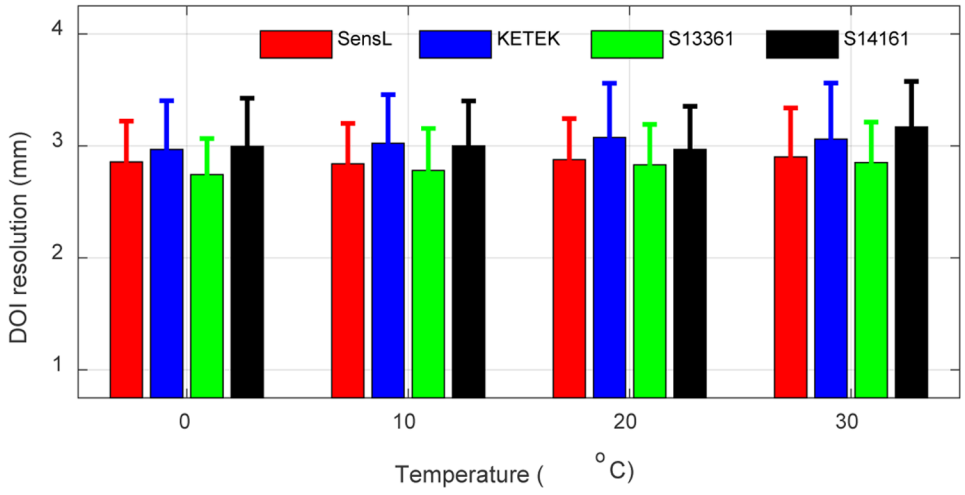

Figure 10.
Average DOI resolution versus temperature.

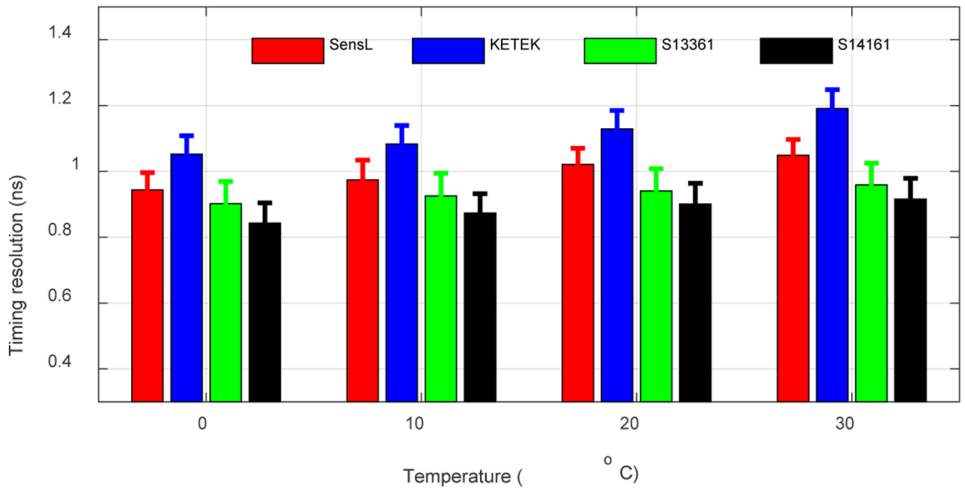

Figure 11.
Average timing resolution versus temperature.

TABLE I

Characteristics of the Sipm Arrays*

	SensL MicroFJ-30035-64P	KETEK PA3325-WB-0808	Hamamatsu	
			S13361-3050NE-08	S14161-3050HS-08
Pitch / mm	3.36	3.36	3.2	3.2
Active area per pixel / mm^2	3.07 × 3.07	3.0 × 3.0	3.0 × 3.0	3.0 × 3.0
Microcell size/ μm	35	25	50	50
No. of microcells / mm^2	630	1547	398	392
Fill factor (%)	75	–– **	74	74
Breakdown voltage (V_{BD}) / V	24.5 ***	27 ***	52 ****	37 ****
Temp. dependency of V_{BD} (mV/ °C)	21.5	22.0	54	34
Signal rise time / ns	0.1	< 1	––	––
Recovery time / ns	37	40	––	––
Spectral response range / nm	200–900	300–900	320–900	270–900
Window material	Glass	––	Epoxy	Silicone
Window refractive index	1.53	––	1.55	1.57
Peak PDE Wavelength (λp)	420	––	450	450

*KETEK 2016a and 2016b, Hamamatsu 2016 and 2017, SensL 2017 and 2018.

**-- Unknown

***Measured at 21 °C.

****Measured at 25 °C.

TABLE II

Experimental Conditions

	SensL MicroFJ-30035	KETEK PA3325-WB	Hamamatsu	
			S13361-3050	S14161-3050
Bias voltage / V	26.5 – 30.0	29.5 – 33.5	53.5 – 58.5	39.0 – 42.5
Temperature / °C		0, 10, 20, 30		

Table III.

The optimal bias voltage for the flood histogram.

Temperature / °C	Bias voltage / V			
	SensL MicroFJ-30035	KETEK PA3325-WB	Hamamatsu	
			S13361-3050	S14161-3050
0	27.5	31.5	55.0	39.5
10	27.5	31.5	55.5	40.5
20	27.5	31.5	56.0	40.5
30	28.0	31.5	57.0	41.0